Aircraft community noise prediction in 3D environments using Gaussian beam tracing

Fuerkaiti, Y.; Casalino, D.; Avallone, F.; Ragni, D.

DOI
10.2514/6.2022-3079

Publication date
2022

Document Version
Final published version

Published in
28th AIAA/CEAS Aeroacoustics Conference, 2022

Aeroacoustics Conferences
June 14-17, 2022, Southampton, UK
28th AIAA/CEAS Aeroacoustics 2022 Conference

10.2514/6.2022-3079

Aircraft community noise prediction in 3D environments using Gaussian beam tracing

Y. Fuerkaiti*, D. Casalino †, F. Avallone ‡, and D. Ragni §
Delft University of Technology, Delft 2629HS, The Netherlands.

This work presents a novel noise propagation approach based on the Gaussian Beam Tracing (GBT) method that accounts for complex source directivity, weather conditions, and irregular ground topology for the evaluation of the noise footprint. The approach takes a precomputed noise sphere as input and propagates the acoustic pressure fluctuations through a moving inhomogeneous atmosphere over realistic three-dimensional (3D) terrain. Noise footprints, obtained with different source noise spheres and wind flow conditions, are compared. It is found that, in a quiescent atmosphere, a change in the source directivity results in a variation up to 15 dB on the acoustic footprint. In the presence of the mean flow, the variation in the noise footprint can reach up to 35 dB. The results suggest that any variation in the source directivity and wind flow can cause a significant change in the acoustic footprint predicted in 3D environments with varying terrain topology and wind flow.

I. Introduction

Aircraft noise has often been regarded as the most undesired sound in urban environment; besides its annoyance, it causes several health issues, for instance, sleep disturbance [1, 2], cardiovascular diseases [3] and altered cognitive performance among children [4]. In the Environmental Noise Guidelines for the European Region (2018) prepared by the World Health Organization (WHO), it was strongly recommended to reduce aircraft noise levels to 45 dB L_{den} (day-evening-night-weighted sound pressure level) and 40 dB L_{night} (night-time equivalent continuous sound pressure level) to protect the health of residents around airports.

In modern megacities, aircraft flyovers around airports feature a moving sound source and long-range propagation affected by range-dependent weather and ground conditions that significantly impact the received noise levels. Therefore, in addition to the mitigation of noise at the source, it is necessary to accurately model noise propagation in a 3D environment considering various atmospheric (refraction, scattering by atmospheric inhomogeneities) and ground effects (multiple reflections, diffraction) and evaluating the impact of noise on the community.

Refraction, i.e., the bending of the propagation paths by wind and temperature gradients, directs the sound energy into certain regions, as illustrated in Fig. 1. When the sound propagates along the wind direction, the sound is refracted downward. Downward Refraction near the ground may combine with ground reflections to create a duct in which acoustic waves propagate in a waveguide instead of radiating in other directions. If the ground surface has a high reflection coefficient (acoustically rigid wall), sound may propagate over long distances with very little loss. When the sound propagates against the wind direction, the sound is refracted upward. A refractive shadow zone, characterized by very low sound levels, may form, as indicated in Fig. 1. At the same time, sound waves are reflected at boundaries between the air, ground, and other obstacles such as buildings, hills, and mountains. In the presence of obstacles, a terrain shadow zone can be formed on the other side of those obstacles with respect to the source location as indicated in Fig. 1. Depending on the wind velocity and temperature gradients, the terrain shadow zone can be enlarged or contracted [5]. If the acoustic wavelength is comparable to the characteristic length of the obstacle, then sound waves can diffract into the terrain shadow and raises noise levels. At the same time, random fluctuations of wind velocity and temperature due to atmospheric turbulent motion result in scattering of acoustic energy into the shadow zones (insonification) and coherence loss of the propagated noise signals. Considering insonification and coherent loss of the noise signals due to atmospheric turbulence requires an additional level of sophistication in the prediction methods, which is not considered in this study.

*Doctoral candidate, Wind Energy Department, y.fuerkaiti@tudelft.nl
†Professor, Wind Energy Department, d.casalino@tudelft.nl
‡Assistant Professor, Wind Energy Department, f.avallone@tudelft.nl
§Associate Professor, Wind Energy Department, d.ragni@tudelft.nl

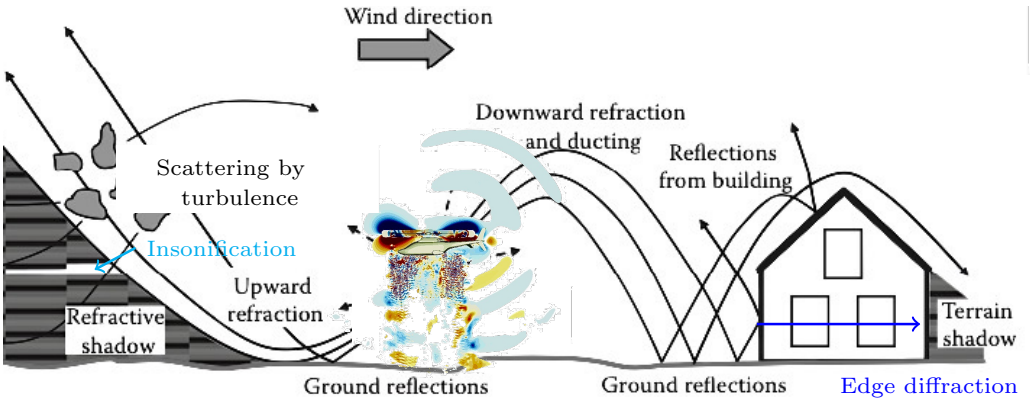

Fig. 1 An illustration of outdoor sound propagation (adapted from [6]).

Over the years, computational tools have been developed to simulate outdoor noise propagation. However, these tools show limitations in including atmospheric and ground effects when applied to the propagation of airborne noise emitted by moving sources over realistic terrains. For instance, Noise-Power-Distance (NPD) data [7], which are specific to each aircraft, have been widely used to evaluate aircraft noise footprint. NPD estimates noise levels for a particular type of aircraft at a given flight condition, e.g., hover and distance from the observer. However, existing NPD data can not be employed to estimate the noise footprint of new aircraft including Urban Air Mobility (UAM) vehicles as they differ in many ways from conventional fixed-wing aircraft or rotary-wing aircraft, e.g., helicopters. Fast Field Program (FFP) [8], on the other hand, can account only for stationary source, layered atmosphere, and a homogeneous ground surface. Methods based on Parabolic Equation (PE) [9] are not optimal when considering moving sources [10] and computationally demanding at high-frequency range. On the other hand, methods based on the solution of wave equations using discretized versions of partial differential equations, such as a finite element or finite difference methods, can include various wave properties (reflection, diffraction, refraction), but they are computationally demanding. Only a few examples are available restricted to relatively low-frequency problems [11, 12]. Contrarily to the methods mentioned above, ray-tracing is a widely used approach for studying sound propagation in a complex environment. The ray-tracing method hypothesizes the existence of wavefronts and the presence of rays that provide a spatial depiction of sound travel and energy flow [5]. Ray-tracing has been shown to provide comparable results to wave-based methods for many high-frequency sound propagation problems. However, it is prone to numerical artifacts such as perfect shadow zone and caustics [13, 14]. Ray-tracing predicts zero level in the shadow zone with a sharp discontinuity at the shadow boundary (perfect shadow zone); it predicts an infinite amplitude at locations where the ray tube cross-section area vanishes (caustics).

Recently, Fuerkaiti et al. [15] developed a two-point 3D eigenray tracer that accounts for sound refraction due to vertical variability of air temperature and wind velocity gradients. Noise footprints of a UAM vehicle cruising at 2 km altitude over a flat ground under different weather conditions were evaluated. A correction model was employed to overcome the perfect shadow zone. Only two contributing rays (one direct and one ground-reflect ray) were considered to discard caustic effects on the acoustic footprint. They reported that the weather significantly impacts long-range propagation, but it plays a small role in short-range propagation distances over flat terrain. However, the work did not address the impact of 3D varying weather conditions and terrain topology on long-range propagation. In a realistic 3D environment, irregularities in local terrain geometries highly distort wind velocity and temperature profiles. Therefore, as mentioned above, various complex propagation phenomena would occur during sound propagation.

The GBT, a high-frequency approximate solution of the wave equation, is a widely used approach for studying wave propagation in a complex environment. Beams are constructed around each ray radiating from a source. The GBT method has two remarkable advantages over classical ray-tracing. First, beams smooth out singularities at caustics and shadow boundaries, thus providing more accurate results. Second, it is more efficient if receivers distributed over a vast area are considered instead of a single receiver because the eigenray connecting the source and a receiver does not need to be identified [16–18]. However, the GBT method does not include diffraction by nature because it assumes the acoustic wavelength is considerably smaller than the characteristic length of any object [19]. Furthermore, the GBT method does not account for complex source directivity. Instead, it assumes an omnidirectional point source such that the amplitude of each beam is identical in all directions. However, it is essential to include the complex source directivity

for aircraft community noise predictions. Recently, Bian et al. [20] proposed a GBT-based model that incorporates complex source directivity by introducing a radiation function in the Gaussian beam summation formulation. However, the approach can not properly project the noise levels from the source onto the ground in the presence of wind flow as the ray-path tracer, which is based on Snell's law, cannot account for the effect of wind velocity and its gradients on the acoustic propagation.

In this work, a new propagation approach based on the GBT method is developed to evaluate the noise footprint of an aircraft in a 3D environment with varying terrain, wind velocity, and temperature profiles. An efficient method is developed in this work to read and evaluate 3D weather profiles. The 3D weather field is approximated by reading the flow data as an ordered combination of 2D field slices sampled along the y-axis in a Cartesian coordinate system. The 2D field slices are sampled at a relatively shorter distance around the building corners, where substantial flow variation can be expected, and at a moderately larger distance if the space between two buildings is big and the variation in the flowfield is not significant. The temperature and wind velocity at any point between two adjacent slices is obtained through barycentric interpolation [21, 22]. Furthermore, a simple and efficient numerical method has been developed in this work to incorporate the complex source directivity without modifying the original beam summation formulation. Apart from the efficiency of the numerical method, it can properly project the corresponding noise levels from the source sphere onto the ground in the presence of strong atmospheric refraction due to wind velocity and temperature variations.

The remainder of this paper is structured as follows. In section II, the methodology is described. In section III, validation and verification results are presented. Section IV shows the application in the noise footprint simulation of a helicopter flying over a mountain. Finally, the conclusion of the work is given in Section V.

II. Methodology

A standard hybrid methodology is used to simulate aircraft noise footprint in a 3D environment. An in-house code universal acoustic ray and Gaussian beam tracer (UYGUR) is developed based on the 3D ray-path tracing method [23], and the GBT method [19, 24]. A schematic illustration of the computational procedures is shown in Fig.2. The terrain geometry, the 3D wind and temperature profiles, and the source spheres are provided as inputs. UYGUR reads terrain geometry in STL file format. In the present version, only regular meshes are considered. The 3D weather data is read as an ordered combination of vertical slices sampled along the y-axis in the Cartesian coordinate system. After reading the environmental profiles, UYGUR performs ray-path tracing in the first step to determine the central ray associated with each Gaussian beam and ray-sphere intersection point. In the second step, each Gaussian beam's initial source magnitude and phase are updated with the ones stored on the ray-sphere intersection point. Next, dynamic ray tracing is carried out to calculate the geometrical spreading and wavefront variation of the sound wave in the vicinity of each ray. Finally, the acoustic field at receiver points is calculated by summing the contribution of each Gaussian beam passing nearby the receiver location.

A. Overview of the GBT approach

The GBT approach adopted in this work is based on well-established ray-tracing and GBT algorithms whose description is beyond the scope of the present work. However, they have never been combined and structured as presented in this work. Some relevant key elements of the formulations and basic steps of the approach are briefly reviewed, while further details can be found in the references [19, 23, 24].

The first step of the GBT is to determine ray-path trajectories in a moving inhomogeneous medium. When the atmosphere is homogeneous and quiescent, an observer sees a wavefront described by $\tau(\boldsymbol{x}) = t$ as a surface that moves with speed $c\boldsymbol{n}$, where t is time, $\boldsymbol{n}$ is normal to the wavefront, and c is the local sound speed. However, when the air moves with velocity $\boldsymbol{v}$, the wavefront has a local speed equal to $d\boldsymbol{x}/dt = \boldsymbol{v}_{ray} = \boldsymbol{v} + c\boldsymbol{n}$. As a consequence, the ray-path vector $\boldsymbol{x}$ follows the direction of $\boldsymbol{v}_{ray}$ instead of $c\boldsymbol{n}$ as indicated in Fig .3a. This work uses the 3D ray-tracing equation derived by Pierce [23] that explicitly incorporates wind velocity, temperature, and their gradients. The 3D acoustic ray-tracing system reads

$$\left.\begin{aligned} \frac{d\boldsymbol{x}}{dt} &= \frac{c^2\boldsymbol{k}}{\Omega} + \boldsymbol{v} \\ \frac{d\boldsymbol{k}}{dt} &= -\frac{\Omega}{c}\nabla c - \boldsymbol{k}\times(\nabla\times\boldsymbol{v}) - (\boldsymbol{k}\cdot\nabla)\boldsymbol{v} \end{aligned}\right\} \tag{1}$$

The derivation of Eq. (1) and the relationships between wave-slowness vector $\boldsymbol{k}$, the unit normal vector to the wavefront $\boldsymbol{n}$, and the parameter Ω are given in [23]. Eq. (1) is solved using a second-order Runge-Kutta scheme.

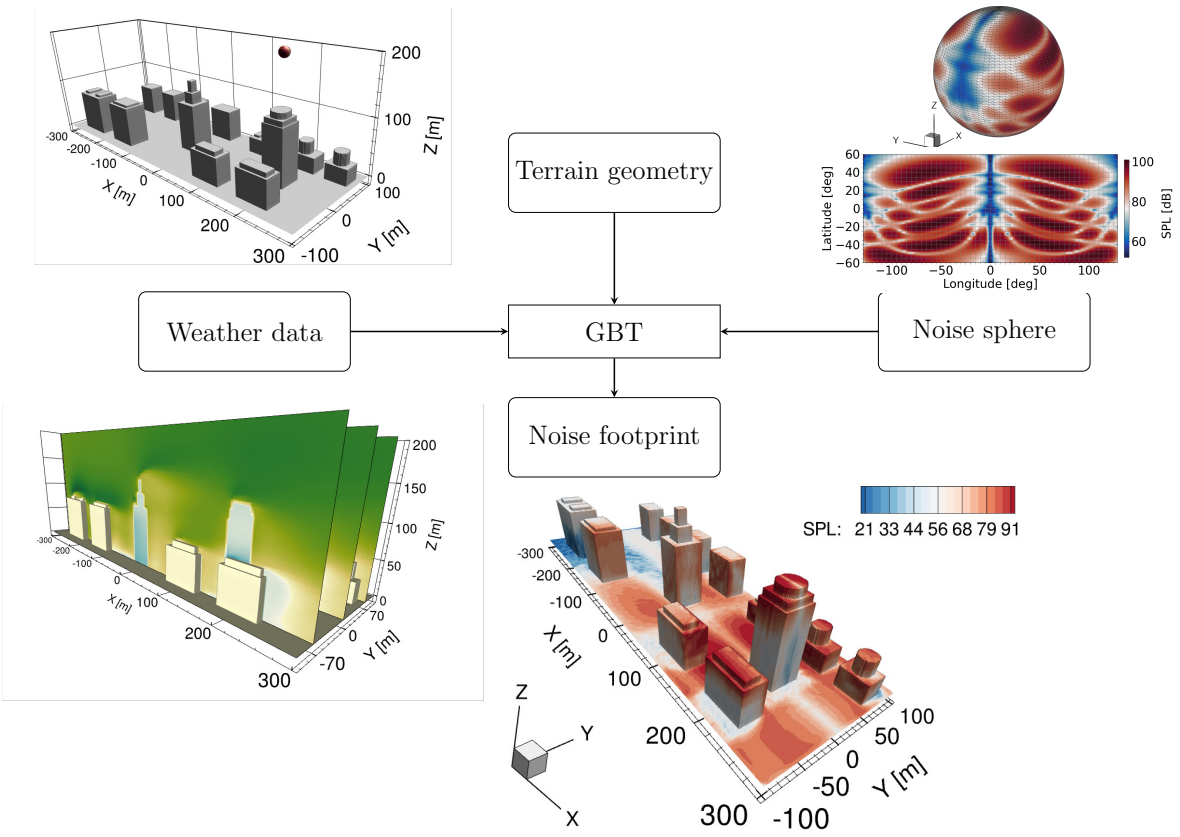

Fig. 2 Schematic illustration of the computational procedures.

Higher-order schemes may be used to get better accuracy. However, as highlighted in [18], higher-order schemes do not improve the GBT results due to the inaccuracies in the environmental details and approximations in the weather profile and boundary interpolation. An adaptive step size strategy is implemented in this work to avoid the computation of redundant ray points that are not relevant to the acoustic pressure field at the receiver locations in interest. For instance, an initial step size, preferred to be a few times shorter than the source height, is used to trace the ray. Whenever the ray interacts with the terrain boundary, the ray step size is reduced iteratively such that it properly lands on the terrain surfaces; consequently, ray paths are finer in the vicinity of the terrain surfaces and coarser farther away from them. Similar approaches have been introduced and implemented in prior works [18, 25] to reduce the computational cost.

The Gaussian beam is then constructed around the central ray (indicated by $\boldsymbol{v}_{ray}$ in Fig. 3) by solving the wave equation locally in ray-centered coordinates using the parabolic approximation. In a 3D medium, the ray-centered coordinates are represented by (q_1, q_2, s), where s is the arc-length along the central ray, and (q_1, q_2) are two normal distances from a field point to the central ray, which are defined as distances in the direction of the two mutually orthogonal unitary normal vectors $\boldsymbol{e}_1$ and $\boldsymbol{e}_2$ to the ray as shown in Fig. 3b. In order to form the Gaussian beams in a 3D environment, it is essential to determine these unitary normal vectors, also known as polarization vectors. Cerveny et al. [26] derived a set of formulations that allows the evaluation of the polarization vectors at any point of a ray. Namely, the polarization vectors are related to the unitary tangent vector $\boldsymbol{t}$ along a ray-path through the ray torsion and curvature, such that $\boldsymbol{e}_1$ and $\boldsymbol{e}_2$ are defined as follows:

$$\begin{bmatrix} e_{1x} \\ e_{1y} \\ e_{1z} \end{bmatrix} = \begin{bmatrix} (ck_1k_3\cos\phi + k_2\sin\phi)/L \\ (ck_2k_3\cos\phi - k_1\sin\phi)/L \\ cL\cos\phi \end{bmatrix}, \quad \begin{bmatrix} e_{2x} \\ e_{2y} \\ e_{2z} \end{bmatrix} = \begin{bmatrix} (ck_1k_3\sin\phi - k_2\cos\phi)/L \\ (ck_2k_3\sin\phi + k_1\cos\phi)/L \\ -cL\cos\phi \end{bmatrix} \tag{2}$$

where $L = \sqrt{(k_1^2 + k_2^2)}$ and ϕ is the rotation angle and given as:

$$\frac{d\phi}{ds} = \frac{k_3(k_2\partial c/\partial x - k_1\partial c/\partial y)}{L^2 c(s)} \tag{3}$$

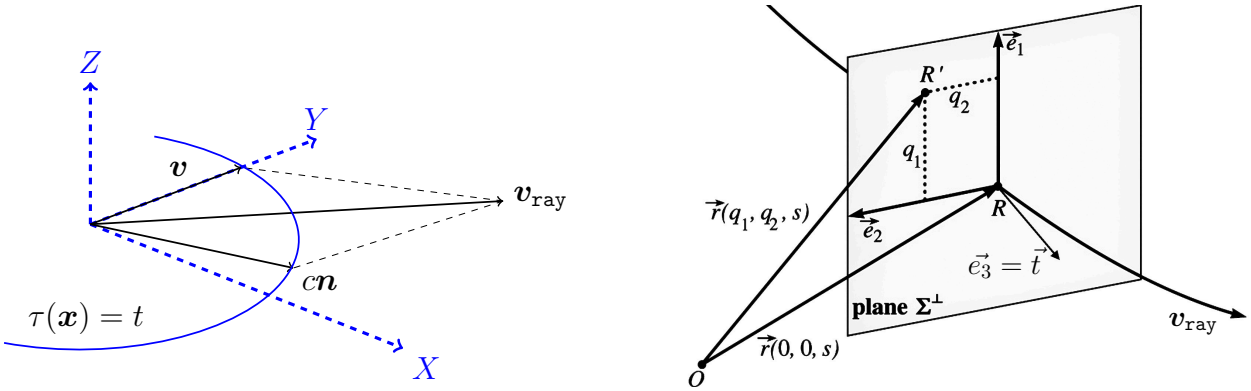

(a) (b)

Fig. 3 Wave normal, wind velocity, and ray-path vector for a moving atmosphere in the Cartesian coordinate system (a). A field point R' situated in the vicinity of a central ray (v_{ray}) in the ray-centered coordinate system (adapted from [19]) (b). The field point R' is located on a plane perpendicular to the central ray crossing at point $s = R$.

With these equations, the polarization vectors can be easily determined at any point of a ray by integrating Eq. (3) together with the 3D ray-tracing system, thus avoiding computation of ray curvature and torsion [26].

The spreading and phase-front change of Gaussian beam along the central ray is governed by the dynamic ray-tracing system given by [27]

$$\left.\begin{aligned} \frac{dp_i}{ds} &= \frac{1}{c^2} c_{i,j} q_i, \quad i,j = 1,2 \\ \frac{dq_i}{ds} &= c p_i \end{aligned}\right\} \tag{4}$$

where p_i describes beam slowness in a plane perpendicular to the propagation path, while q_i describes the beam spreading in the vicinity of the central ray along the propagation path, $c_{i,j}$ is a matrix of second derivatives of sound speed with respect to the two normal distances q_1 and q_2.

$$c_{i,j} = \begin{bmatrix} \dfrac{\partial^2 c(s)}{\partial q_1^2} & \dfrac{\partial^2 c(s)}{\partial q_1 \partial q_2} \\ \dfrac{\partial^2 c(s)}{\partial q_2 \partial q_1} & \dfrac{\partial^2 c(s)}{\partial q_2^2} \end{bmatrix} \tag{5}$$

Two linearly independent solutions are considered to obtain the Gaussian beam in a 3D environment [24] with the initial conditions

$$\begin{bmatrix} \boldsymbol{P}(0) \\ \boldsymbol{Q}(0) \end{bmatrix} = \begin{bmatrix} p_1^{(1)}(0) & p_1^{(2)}(0) \\ p_2^{(1)}(0) & p_2^{(2)}(0) \\ q_1^{(1)}(0) & q_1^{(2)}(0) \\ q_2^{(1)}(0) & q_2^{(2)}(0) \end{bmatrix} = \begin{bmatrix} 1 & 0 \\ 0 & 1 \\ \epsilon_1 & 0 \\ 0 & \epsilon_2 \end{bmatrix} \tag{6}$$

where $\epsilon_{1,2}$ are complex numbers that control the initial beamwidths in the two normal directions to the ray. The real and imaginary parts of $\epsilon_{1,2}$ allow independent control of both the beam width and the beam curvature. Once these equations

are integrated along the central ray, the Gaussian beam can be formed as [19, 24]

$$u_b(q_1, q_2, s) = \frac{A(s)}{\sqrt{|\boldsymbol{Q}|}} e^{i\omega[\tau(s)+0.5\boldsymbol{q}^T\boldsymbol{\Gamma}(s)\boldsymbol{q}]} \tag{7}$$

where $A(s)$ is the beam amplitude at s, $\tau(s)$ is the travel-time along the central ray, $\boldsymbol{\Gamma}(s) = \boldsymbol{P}(s)\boldsymbol{Q}^{-1}(s)$ is the 2×2 matrix of the second derivatives of the travel-time field with respect to the ray-centered coordinates and $\boldsymbol{q} = (q_1, q_2)^T$ is the distance vector. For a complete derivation of dynamic ray tracing, readers can refer to the book of Cerveny [19] and Popov [24].

When beams interact with environmental boundaries like irregular ground surfaces, terrain boundaries, etc., there is a jump in the sound speed gradient due to the discontinuity in the medium density such that the quantities $p_{i,j}$ and $q_{i,j}$ $(i, j = 1, 2)$ change considerably across those boundaries [27]. Hence, at points of incidence of a ray at an interface, the values of $p_{i,j}$ and $q_{i,j}$ must be updated. These new values will serve as the initial values for the solution of the dynamic ray tracing equations along with rays of reflected or transmitted waves. In this work, the formulae derived by Popov et al. [27] were used to update $p_{i,j}$ and $q_{i,j}$ at the points of incidence.

The final step of GBT is a superposition of all contributing Gaussian beams in the neighborhood of the receiver R'. The total field at a point located at the receiver R' reads

$$U(R', \omega) = \int \int \Phi(\alpha, \beta, \omega) u_b(q_1, q_2, s) d\alpha d\beta \tag{8}$$

where α and β are the shooting angles in the elevation and azimuthal direction, respectively, of a ray with respect to an arbitrary axis passing through the source and $\Phi(\alpha, \beta, \omega)$ is called the weighting function. The weighting function is calculated by expanding the wavefield at the source and matching the high-frequency asymptotic behavior of the integral in Eq. (8) to the exact solution for a source in a homogeneous medium where the ray field is regular.

B. Inclusion of complex source directivity into the acoustic footprint

In UYGUR, each Gaussian beam has the same initial amplitude and phase. Inclusion of complex source directivity into the acoustic footprint follows similar steps as described in [15]. In this work, those steps are adapted for the GBT procedures and briefly explained in the following. In the first step, UYGUR reads a precomputed noise sphere representing the frequency, magnitude, and phase of noise signals radiated by noise sources over a range of directions for a particular flight condition. In the second step, the central ray-path trajectories and ray-sphere intersection points are determined simultaneously by employing the 3D ray-tracing system [23]. In the third step, each Gaussian beam's initial phase and magnitude are updated with the ones stored on the ray-sphere intersection point and projected on the ground with the dynamic ray tracing procedure. One of the advantages of this method is that it can accurately propagate the noise levels on the acoustic sphere onto the ground even in the presence of strong atmospheric refraction. In this case, sound rays curve more with increasing propagation distances resulting in the shift of the ray-sphere intersection point, as illustrated in Fig. 4. For instance, the ray-sphere intersection points corresponding to a direct and ground reflected rays are shifted from s and s' to c and c', respectively, in the presence of wind flow.

III. Validation and Verification

The GBT model was assessed in the previous work from Fuerkaiti et al. [15] by comparing it against an exact solution that describes the elementary sound propagation problem in a homogeneous atmosphere over flat terrain. In this work, UYGUR's capability to include complex source directivity is verified by comparing the acoustic footprint of a twin-propeller against reference data that was generated by *Optyð B*-FOOTPRINT tool [28]. Afterward, multiple reflections in an urban setting are validated by comparing GBT-based predictions against a full-wave solution. For this purpose, the *Optyð B*-GFD tool that solves the Helmholtz equation using the Finite Element Method (FEM) is used to generate reference data. Lastly, range-dependent refraction due to 3D varying wind flow is validated by comparing the result against the reference predictions with a mean flow.

A. Inclusion of complex source directivity into acoustic footprint

The source noise hemisphere is computed with the efficient low-fidelity approach [28] for a twin-propeller configuration operating at 2km, with an advance ratio $J = 0.84$. The distance between propellers is $2D_p$ (D_p propeller

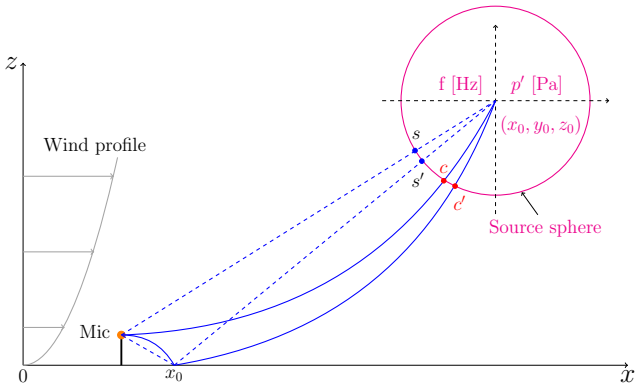

Fig. 4 Illustration of inclusion complex source directivity and projection noise levels from source sphere to the ground observer. Dashed lines represents sound rays in a quiescent, homogeneous atmosphere, while curved solid lines represent the sound rays in a windy atmosphere.

diameter), and the phase angle is 0°. The noise hemisphere radius is $10D_p$. It is assumed that both propellers operate at the same RPM. The bottom view of the noise hemisphere for the first harmonics of BPF is shown in Fig.5a. The interference pattern due to the acoustic interaction of these two propellers is clearly visible on the source hemisphere. The reference noise footprint is obtained by projecting the noise levels from the source hemisphere onto the ground receivers using the *Opty∂B*-FOOTPRINT tool that propagates the sound rays towards the ground using straight rays [15, 29]. The receivers are distributed over a square area of 2.5 km by 2.5 km, as illustrated in Fig. 5b. The noise footprints predicted with UYGUR and *Opty∂B*-FOOTPRINT are compared and displayed in Fig.5c and Fig 5d, respectively. A favorable agreement is observed between the two that verifies the reliability of UYGUR for the inclusion of complex source directivity.

B. Multiple reflection and range-dependent refraction

1. Reference solution

The reference solution for this specific validation is obtained by using the frequency-domain FEM acoustic solver *Opty∂B*-GFD and solving a second-order wave equation for the perturbation velocity potential in a non-uniform flow. This specific study uses an immersed boundary technique for automatic mesh generation. The immersed boundary method relies on the intrinsic capabilities of a finite-element scheme of decoupling the nodes at which the solution is calculated from the points where an equation is satisfied. Therefore, the zero-normal derivative equation of the perturbation velocity potential (slip condition) is satisfied at the exact points of the imported immersed geometry, using the exact value of the surface normal. In order to improve the capability of the method to take into account the diffraction of an edge, when one mesh volume element is crossed by a wedge, one or more mutually unconnected virtual nodes are added to the volume mesh by duplication, and an equal number of new equations are added to the system. Every additional equation corresponds to the slip condition with a local value of the surface normal. The FEM code *Opty∂B*-GFD has been validated for a variety of canonical problems [30–32] involving acoustic propagation in uniform and non-uniform flows, and its complete description is outside the scope of the present work.

2. Case setup

An urban setting with three building blocks is considered to validate the present noise propagation approach for multiple reflections and range-dependent refraction. All three building blocks have the same dimension. The building length L_B is set to 4 m. The urban boundary is considered to be a perfect reflector; hence no acoustic energy is absorbed by the boundaries. The dimensions of the computational domain and the building blocks are listed in Table. 1.

A time-harmonic monopole source with source frequencies 200 Hz located at $(12.5, 0, 4.5)L_B$, is considered. The acoustic wavefield is investigated on two different receiver planes: XZ-plane at Y = 0 m and XY-plane at Z = $2.5L_B$. Examples of source-receiver geometry for the three-building configurations are displayed in Fig. 6.

For the given source frequencies, the permanent matching layer (PML) thickness in the reference solution is set to

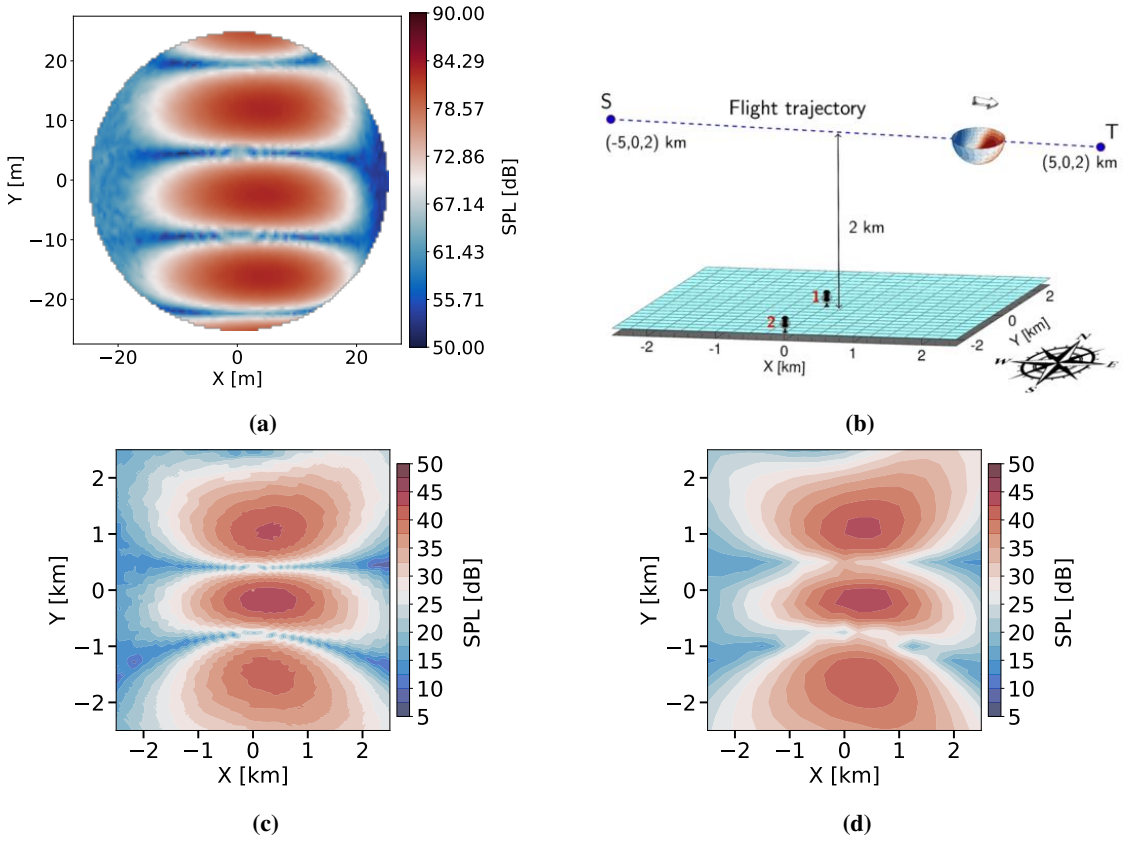

Fig. 5 Bottom view of a reference noise hemisphere of a twin-propeller configuration (a). Geometry of the problem (b). Noise footprint computed with UYGUR (c) and *Opty∂B*-FOOTPRINT (d).

$0.5L_B$ to prevent any contamination due to possible reflected waves from the domain boundaries and ensure the PML absorbs acoustic energy properly. Moreover, the domain is discretized considering 9 points per wavelength to capture the wave interference pattern correctly. The GBT and FEM tools run on an Intel(R) Xeon(R) Gold 6140 CPU @2.3 GHz processor with 36 cores.

Two weather conditions, a windy and a quiescent atmosphere with a constant temperature of 15 °C are considered. The wind flow in the computational domain is resolved using the high-fidelity CFD solver SIMULIA PowerFLOW® based on the Lattice Boltzmann Very Large Eddy Simulation (LB/VLES) method, which is inherently unsteady and relies on an explicit time marching algorithm. One of the advantages of using PowerFLOW® for urban wind simulations consists in the full automation of the volume mesh generation, which is created by the software around the imported geometries, by following user-defined regions of Variable Resolution (VR). A Cartesian mesh is employed by the Lattice-Boltzmann scheme with a resolution jump of factor 2 between adjacent VRs. In every VR, the time marching algorithm uses a local time step, thus resulting in a rate that is twice faster in a twice finer resolution region. The calculation load is automatically balanced among processors based on the so-called fine-equivalent number of voxels, i.e., the number of voxels multiplied by the ratio between the local resolution and the maximum resolution level.
Three VRs are used, with the smallest voxel size of $0.0167L_B$. This results in a total voxel count of 72 million, with 70 million fine-equivalent voxels. The VRs are placed onto regions of interest, e.g., around the building edges. The initial velocity is set to 5 m/s at the inlet, and the wind direction points to the positive x-axis direction. The mean flow required by the GBT and reference calculations is then acquired by time-averaging flow data sampled at multiple time frames. A snapshot of the mean flowfield on the vertical receiver plane for the three-building configuration is displayed in Fig. 6c.

Table 1 Dimensions of the computational domain and building blocks.

Domain	x [m]	length [m]	y [m]	width [m]	z [m]	height [m]
Computational domain	[0, 60]	$15L_B$	[-10, 10]	$5L_B$	[0, 20]	$5L_B$
Building 1	[8, 12]	L_B	[-4, 4]	$2L_B$	[0, 12]	$3L_B$
Building 2	[28, 32]	L_B	[-4, 4]	$2L_B$	[0, 12]	$3L_B$
Building 3	[36, 40]	L_B	[-4, 4]	$2L_B$	[0, 12]	$3L_B$

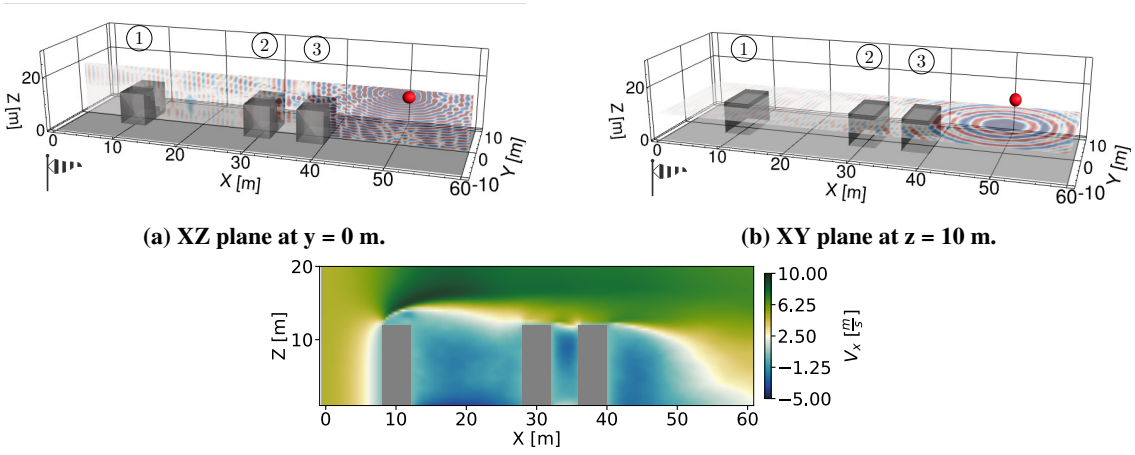

(a) XZ plane at y = 0 m.

(b) XY plane at z = 10 m.

(c) Mean flow.

Fig. 6 Source receiver geometry in a three-building environment. Vertical receiver plane at $Y = 0$ m (a). Horizontal receiver plane at $Z = 2.5L_B$ (b). Snapshot of the mean flow field on the vertical receiver plane (c). Wind direction points to the positive x-axis.

3. Multiple reflections in homogeneous and quiescent atmosphere

The comparisons between the two approaches at different observation planes are displayed in Fig. 7. GBT can capture the the interference pattern except for those between two adjacent building blocks. This is due to the diffracted sound waves into the building canyons, which are present in the reference result and are not included in the GBT model. The discrepancies at the receivers closer to the source are attributed to distortion of the pressure field by the diffracted sound waves from the edges of the third building closer to the source location in the reference result. The line plots showed a favorable agreement between the two approaches in terms of the pressure magnitude. The disparity in the phase is again attributed to the diffraction effects, which are not included in the GBT predictions.

4. Multiple reflection and refraction in the presence of mean flow

The acoustic pressure field computed with the two approaches are compared on the vertical and horizontal receiver planes and displayed in Fig. 8. In the presence of the wind flow, UYGUR is able to capture the general trend of the reference result except at two locations where the GBT prediction deviates clearly from the FEM solution. The first location is the region enclosed by X=[30, 50] m and Z=[16, 18] m, where UYGUR predicts larger pressure fluctuations due to large wind speed gradients at the roof level, as displayed in Fig. 6c. Therefore, sound waves propagate in a refractive waveguide formed by the large wind speed gradients instead of radiating in other directions. As pointed out by Porter [18], Cervenỳ [19], although the evaluation of rays passing through a refractive waveguide is more straightforward, however, the accuracy of the wavefield computations with the GBT method drops drastically if the wavelength is not much smaller than the dimension of the waveguide. The second location is the region inside the second and third buildings, where UYGUR predicts a too small pressure amplitude. However, a strong pressure oscillation is visible in the reference result due to the formation of a standing wave with a large amplitude oscillation. A remarkable improvement in the GBT prediction is observed when comparing the line plots with and without the mean flow. This is because of the

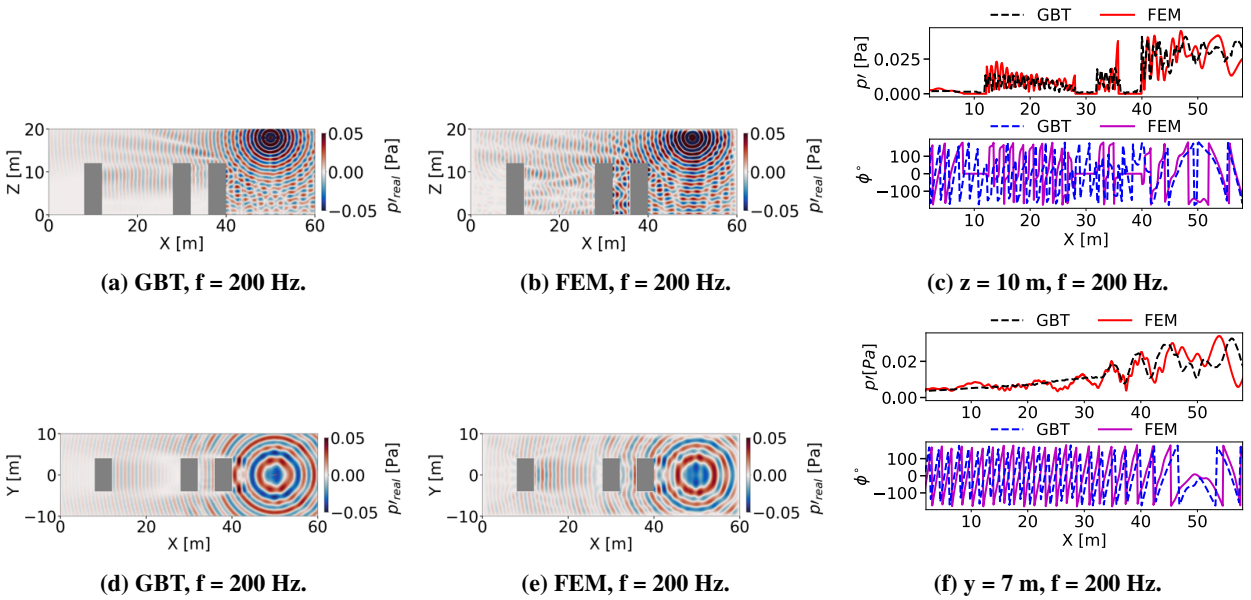

(a) GBT, f = 200 Hz. **(b) FEM, f = 200 Hz.** **(c) z = 10 m, f = 200 Hz.**

(d) GBT, f = 200 Hz. **(e) FEM, f = 200 Hz.** **(f) y = 7 m, f = 200 Hz.**

Fig. 7 Comparison of UYGUR (GBT) and *Opty∂B*-GFD (FEM) on the vertical and horizontal observation planes.

dependence of diffraction on the acoustic wavelength. When sound propagates against the wind, the wavefront has a local speed that decreases along a ray path. The reduction in the local sound speed decreases the wavelength such that the diffraction becomes less evident, which enhances the agreement between the two approaches. It is also observed that acoustic pressure amplitude decreases considerably inside the first and second building, which is well captured by the GBT prediction, highlighting the significant impact of 3D mean flow on acoustic propagation. The GBT prediction will lead to totally unrealistic results if the effect of wind flow is not considered or approximated by analytical formulations such as range-independent logarithmic or constant gradient weather profiles.

From the comparison on the horizontal receiver plane it is seen that in the presence of the mean flow, the GBT approach can capture the general trend of the interference pattern of the reference solution. However, the GBT predictions decay considerably at receivers located farther away from the source in the upstream direction and rise noticeably downstream direction. The line plot on the horizontal receiver plane further highlights the impact of refraction on the diffraction, particularly in terms of the phase of the complex pressure, as an excellent agreement is obtained.

A good agreement is found between the two approaches. It should be noted that GBT is a high-frequency approximate solution of the wave equation that can give satisfactory results compared with the wave-based methods for higher frequency problems. However, the sound waves can be diffracted into the shadow regions behind the building blocks for lower frequencies, altering the field's interference pattern. Furthermore, refraction may either enhance or reduce the effect of diffraction as the wavelength of the local sound wave varies during propagation. Consequently, one may expect a slight deviation in the GBT prediction concerning the reference result. In the following, UYGUR is applied to predict the noise footprint of a helicopter vehicle hovering over a mountain.

IV. Helicopter noise footprint in a 3D environment

In this section, UYGUR's capability of including complex source directivity, multiple reflections due to irregular terrain surfaces, and refraction due to 3D variation in the wind flow is demonstrated by computing the noise footprint of a helicopter hovering over a mountain. The influences of varying source directivity, local terrain and weather conditions on the noise footprint are studied.

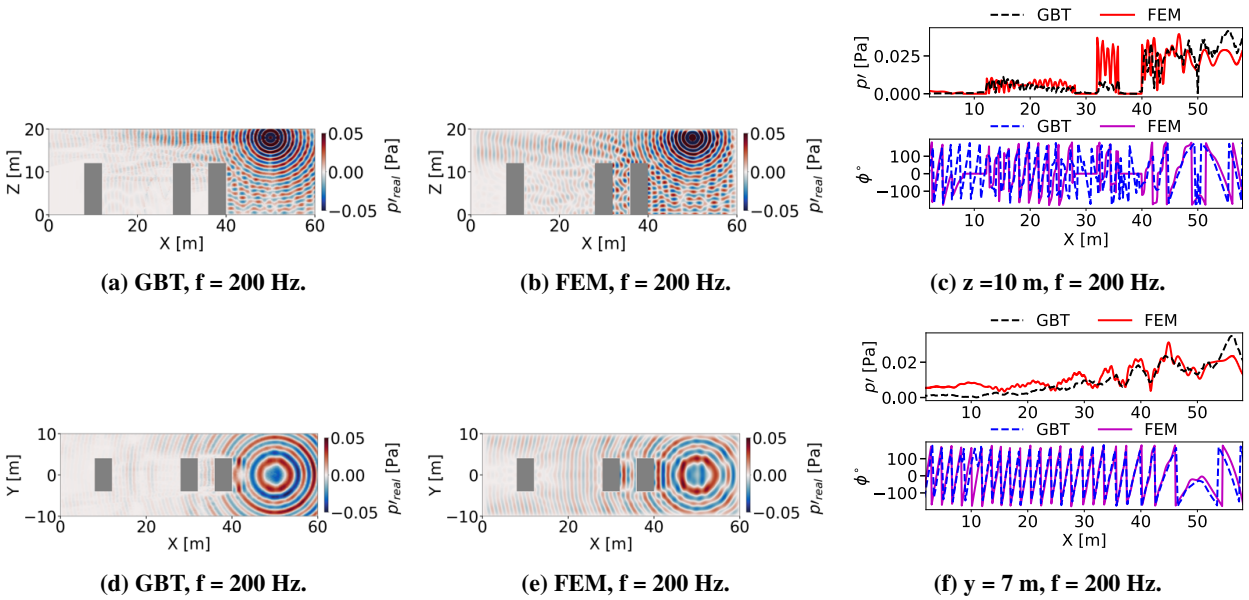

(a) GBT, f = 200 Hz. **(b) FEM, f = 200 Hz.** **(c) z =10 m, f = 200 Hz.**

(d) GBT, f = 200 Hz. **(e) FEM, f = 200 Hz.** **(f) y = 7 m, f = 200 Hz.**

Fig. 8 Comparison of UYGUR (GBT) and *Opty∂B*-GFD (FEM) on the vertical and horizontal receiver plane in the presence of moving medium.

A. Case description and input files

1. Source noise directivity

The helicopter geometry considered in this study was designed by Dassault Systemes and delivered as part of the helicopter automatic simulation workflow of SIMULIA PowerFLOW®. The helicopter is driven by a main rotor and a tail rotor; the tail rotor is mounted on the starboard side, as shown in Fig. 9a. The geometrical specification of the vehicle and operational conditions for the case under consideration are listed in Table 2. The noise sphere is defined in the vehicle reference system (zero pitch, yaw, and roll), as shown in Fig. 9b. The noise sphere radius R_h is set to 6 times the length of the fuselage to ensure the flow pressure is fully recovered, and only the acoustic pressure exists on the surface of the sphere. 32 meridians and 32 parallels are used to discretize the sphere to capture the complex source directivity on the sphere. The source noise spheres are calculated by employing the FW-H solver of SIMULIA PowerACOUSTICS® on the scale-resolved flow data obtained with PowerFLOW®. Here, the source noise spheres corresponding to the fifth and tenth harmonics of the main rotor Blade Passing Frequency (BPF) 20 Hz are considered. The resulting acoustic spheres are plotted using the equidistant cylindrical projection [33] and displayed in Fig. 9c and Fig. 9d, respectively. The tail rotor's contribution to noise levels on the source sphere is clearly visible for the 5 BPF, while it is not apparent for the 10 BPF.

2. Terrain geometry and wind flow

The mountain geometry is obtained by running a python script developed in 3DS Dassault Systems that can extract the earth's elevation using the Shuttle Radar Topography Mission (SRTM) database for given coordinates. The python script exports the terrain geometry in STL format that UYGUR can directly read. The mountain geometry is exported in a square area of 2500 m by 2500 m and is shown in Fig. 10. The highest point of the mountain is 2153 m. Receivers are distributed on the mountain's surface with 30 m spacing in x and y directions. To investigate the acoustic impact of variations in the source directivity, wind flow, and the mountain geometry, noise levels at six particular locations, as indicated in Fig. 10, are considered. The helicopter hovers at (1500, 700, 2300) m, where the impact of the mean flow on the noise signals sampled on the surface of the sphere is assumed to be negligible. The wind field in the computational domain is resolved using the high-fidelity CFD solver SIMULIA PowerFLOW® for an initial wind velocity of 6 m/s that points to the positive X-axis direction. Snapshots of the wind field on the XZ-plane at Y = 700 m and the XY-plane at Z = 2300 m are displayed in Fig. 10(b) and Fig. 10(c), respectively, that show how the mountain geometry distort the wind field.

Table 2 Specifications and operational conditions of the case under investigation.

Main rotor blade tip Mach number (M)	0.51	-
Main rotor rotational speed	300	RPM
Tail rotor rotational speed	1500	RPM
Estimated gross weight	3567.0	kg
Fuselage length (L)	10.6	m
Main rotor diameter (D_m)	10.7	m
Tail rotor diameter (D_t)	2.12	m
Main rotor blade number (NB)	4	-
Tail rotor blade number (NB)	2	-
Main rotor hub-to-tip ratio	0.0561	-
Tail rotor hub-to-tip ratio	0.2682	-
Flight Altitude	2300	m

Three cases that feature the acoustic effects of varying source directivity and wind flow on the noise footprint are considered. All cases share the same total thrust of 35000 N. The test matrix for this analysis is listed in Table 3.

Table 3 Test matrix for the case study.

Case #	main rotor BPF [Hz]	atmosphere
1	100	quiescent
2	200	quiescent
3	100	windy

B. Results

1. Acoustic impact of varying source directivity on the long-range propagation

The acoustic impact of varying source directivity on the long-range propagation is evaluated by comparing the noise footprints calculated for Case 1 and Case 2. As seen in Fig. 11a, in Case 1, the other side of the mountain is predicted as a terrain shadow except for region A. This is due to region A being relatively elevated with respect to its neighborhood; hence, it is still in the illuminated zone concerning the source location. However, noise levels dropped considerably in region A in Case 2, as shown in Fig. 11b, even if it is in the illuminated zone. This is attributed to the variation in the source directivity; the lower noise levels on the sphere are projected into region A. The field difference between the two cases is calculated and displayed in Fig. 11c. As seen, the noise levels in region A reduced up to 15 dB when the BPF increased. Similar trends are observed for regions B and C. Furthermore, in Case 2, the terrain shadow zone predicted in region D appeared to be expended. In fact, the lower noise levels on the noise sphere are projected on region D; thus, the shadow zone seems to be expanded in region D. Moreover, the noise levels in region F, particularly in the area around the edge of the domain, dropped significantly, which is again attributed to the variation in the source directivity. The results suggest that receivers in the illuminated zone and around the terrain shadow zone can experience totally different noise levels when source directivity changes.

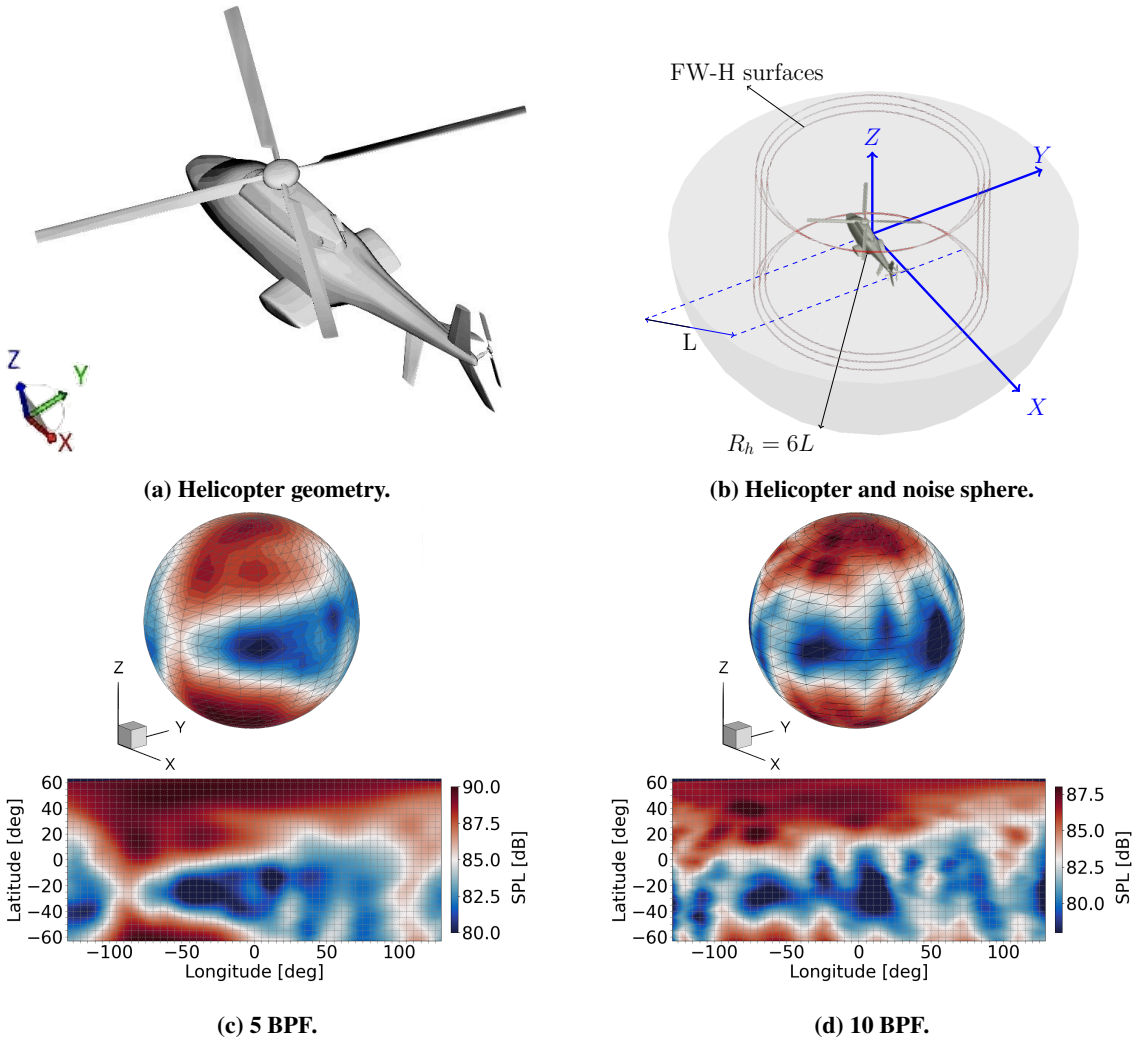

(a) Helicopter geometry.

(b) Helicopter and noise sphere.

(c) 5 BPF.

(d) 10 BPF.

Fig. 9 3DS helicopter model for hover (a), including the mearmeable smapling surfaces for FW-H acoustic propagation and noise sphere (b). Source noise spheres calculated for the 5 BPF (c) and 10 BPF (d) of the main rotor.

2. Acoustic impact of the wind flow on the long-range propagation

The acoustic impact of mean flow on the long-range propagation is studied with Case 2 and Case 3. The noise footprint for Case 3 is calculated and displayed together with the field difference in Fig. 12. As seen in Case 3, noise levels in regions A, B, and C are decreased considerably due to the upward refraction, which forms the refractive shadow zone. In a non-turbulent medium, the effectiveness of the refractive shadow zone increases with increasing propagation range [15]. As highlighted in [5], in the presence of wind flow over the mountain, the terrain shadow zone can be enlarged with upward refraction or contracted with downward refraction, depending on the wind direction. In Case 3, for instance, the terrain shadow zone is enlarged due to upward refraction; hence, noise levels in regions A and B dropped about 30 and 23 dB, respectively. A significant reduction in the noise levels at region C is also observed. This is attributed to the following two reasons: First, there is still substantial upward refraction due to the large wind speed gradients (see Fig. 10) even though region C is closer to the source location. Second, noise levels on the source sphere are shifted to the negative y-axis and positive x-axis directions as ray-sphere intersection points are changed due to the atmospheric refraction effects [15]. The terrain shadow zone in region D is slightly contracted due to downward refraction and shifted to the negative y-axis direction. Higher noise levels are observed in regions E and F for two reasons: First, downward refraction increases noise levels as multiple reflections can occur due to sound rays with lower

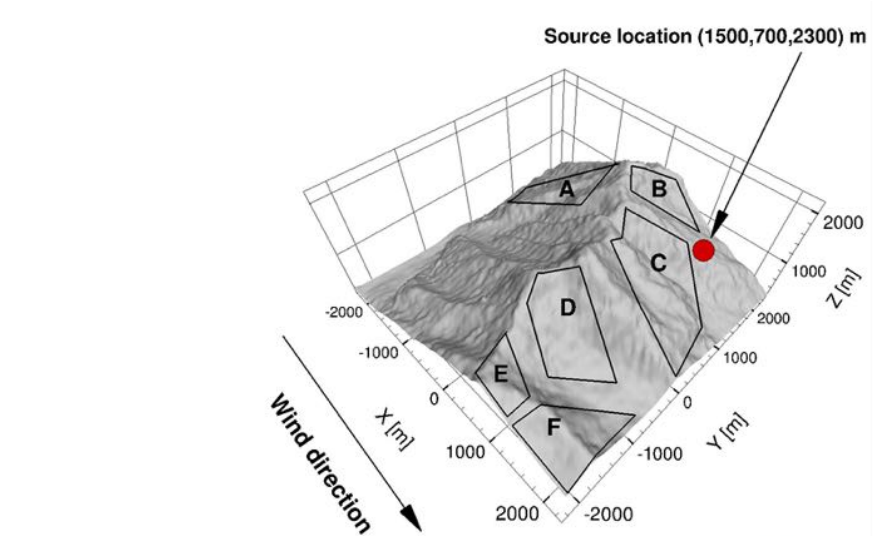

(a) Geometry of the problem.

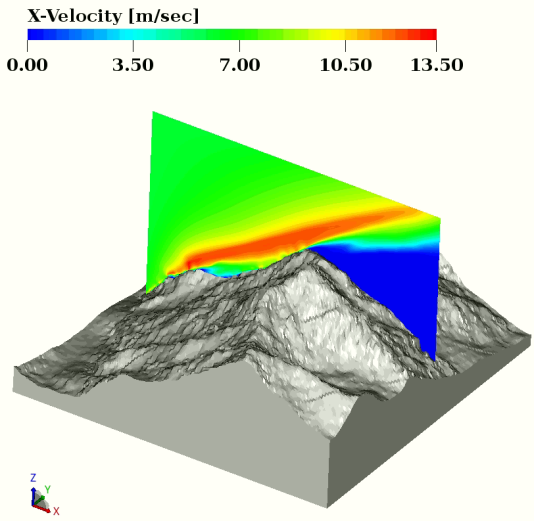

(b) Mean flow on XZ-plane at Y = 700 m.

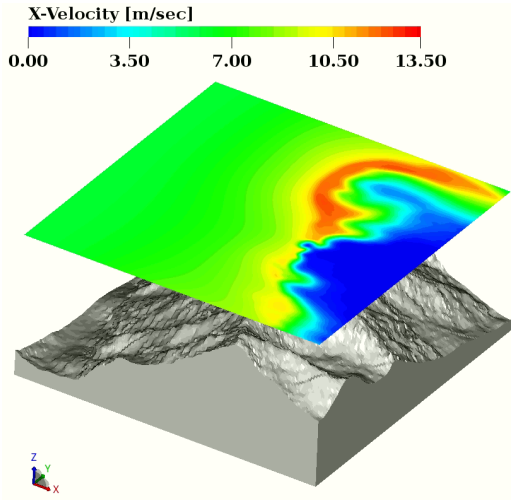

(c) Mean flow on XY-plane at source height.

Fig. 10 Geometry of the problem (a). Snapshots of the mean flow on XZ plane at Y = 700 m (b) and on XY-plane at the source height (c).

grazing angles (sound waves refracted towards the ground and reflected off the ground). Second, due to the atmospheric refraction, sound rays become more curved with increasing propagation range [15]. Thus, the ray-sphere intersection points are shifted to another point with a different phase and magnitude, which eventually alters the projected noise levels on the ground.

In reality, the field differences could be lower than those estimated in this work. In the present study, for instance, the terrain surface is assumed to be a perfect reflector which is another factor that increases noise levels in a downward refracting medium [6, 34]; however, as pointed out in [34] the soil composition plays a significant role like the ground topology in sound propagation, altering the noise levels and its spatial distribution.

V. Conclusion

A new propagation approach based on GBT that includes complex source directivity, sound wave refraction, and multiple reflections due to the variation in the weather conditions and ground topology, respectively, is developed and

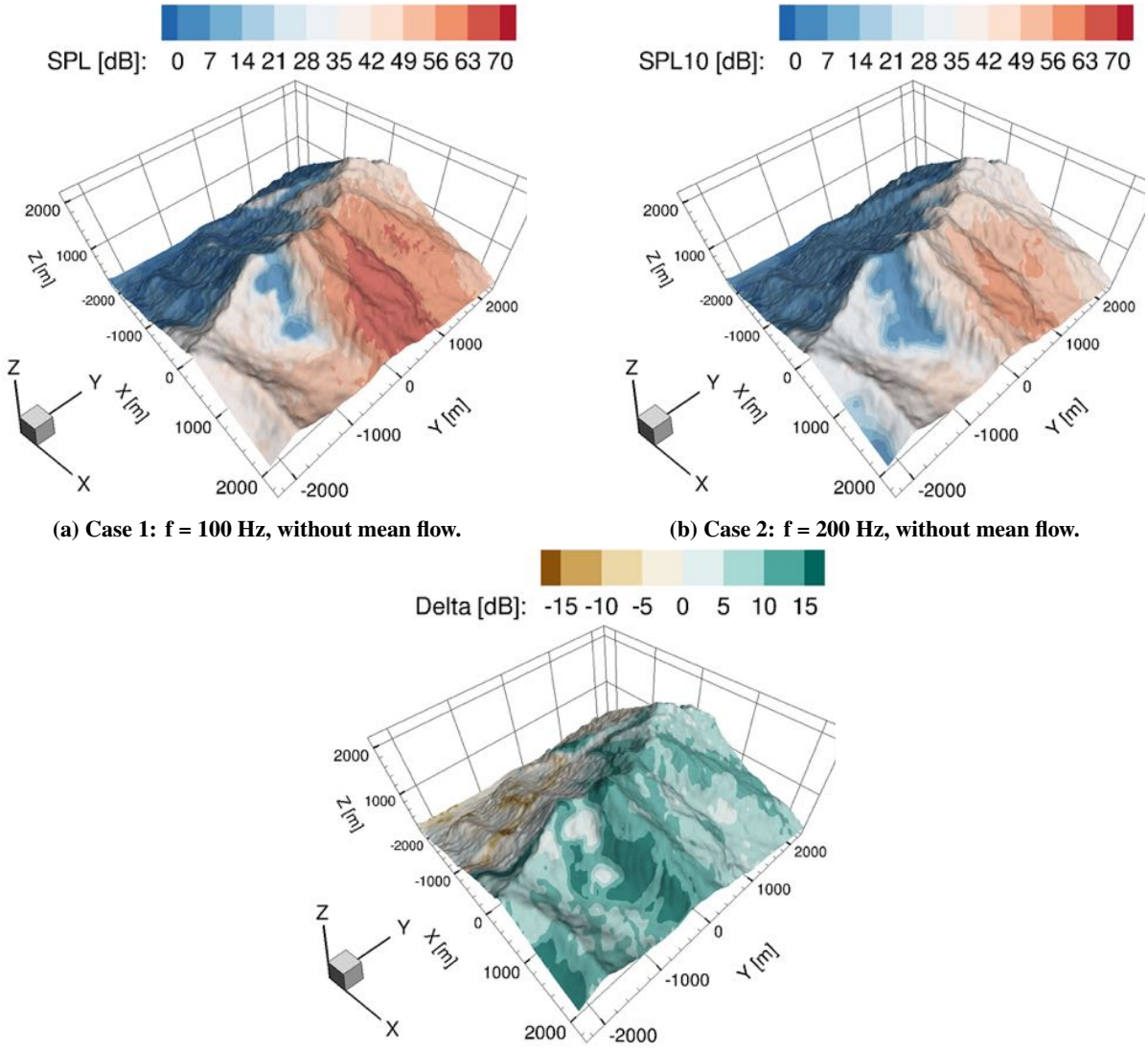

(a) Case 1: f = 100 Hz, without mean flow.

(b) Case 2: f = 200 Hz, without mean flow.

(c) Delta Case 1-2.

Fig. 11 Noise footprint calculated for Case 1 (a) and Case 2 (b). The field difference is calculated by subtracting the noise levels in Case 2 from Case 1. The negative values indicate higher noise levels in Case 2.

presented in this work. The outlined approach can accurately predict the acoustic pressure field behind the obstacles; however, it failed to simulate the pressure field in the illuminated zone when the acoustic wavelength is comparable with the characteristic length of the obstacle. The proposed approach is then applied to study the acoustic impact of varying source directivity and wind flows on the noise footprint of a helicopter hovering over a mountain. It is found that in a quiescent atmosphere, a change in the source directivity resulted in a variation up to 15 dB on the acoustic footprint. In the presence of the mean flow, the variation in the noise footprint can reach up to 35 dB.

The results suggest any variation in the source directivity and wind flow can cause a significant change in the acoustic footprint predicted in a long-range propagation environment with 3D varying terrain topology and wind flow. Furthermore, on-ground noise levels at particular locations can be reduced significantly by providing reliable weather and terrain data.

The GBT method presented in this paper does not account for the influence of atmospheric turbulence on sound propagation. More sophisticated models are needed to include the insonification of the refractive shadow zone due to sound scattering by atmospheric turbulence. Furthermore, the terrain surface is assumed to be an acoustically rigid wall; more comprehensive models are needed to include sound energy absorption due to different ground impedance and soil

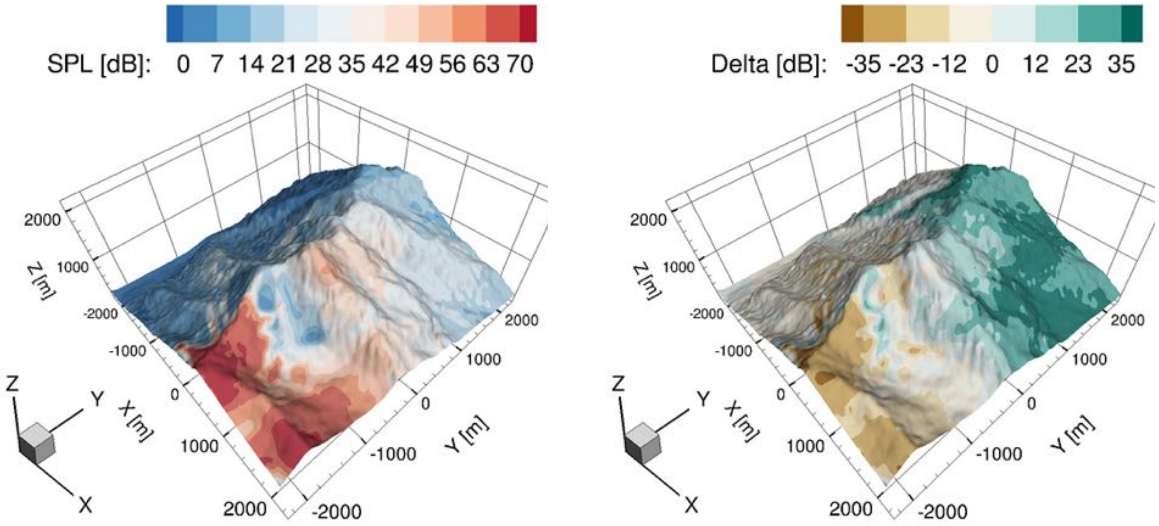

(a) Case 3: f = 100, with mean flow. **(b) Delta Case 1-3.**

Fig. 12 Noise footprint calculated for Case 3 (a) and the field difference between Case 1 and Case 3 (b). The negative values indicate higher noise levels in Case 3.

composition.

Acknowledgements

The authors would like to thank Wouter van der Velden for sharing the python script to extract the terrain geometry.

References

[1] Basner, M., and McGuire, S., "WHO environmental noise guidelines for the European region: a systematic review on environmental noise and effects on sleep," *International journal of environmental research and public health*, Vol. 15, No. 3, 2018, p. 519.

[2] Nassur, A.-M., Lefèvre, M., Laumon, B., Léger, D., and Evrard, A.-S., "Aircraft noise exposure and subjective sleep quality: the results of the DEBATS study in France," *Behavioral sleep medicine*, Vol. 17, No. 4, 2019, pp. 502–513.

[3] Van Kempen, E., Casas, M., Pershagen, G., and Foraster, M., "WHO environmental noise guidelines for the European region: a systematic review on environmental noise and cardiovascular and metabolic effects: a summary," *International journal of environmental research and public health*, Vol. 15, No. 2, 2018, p. 379.

[4] Evrard, A.-S., Bouaoun, L., Champelovier, P., Lambert, J., and Laumon, B., "Does exposure to aircraft noise increase the mortality from cardiovascular disease in the population living in the vicinity of airports? Results of an ecological study in France," *Noise & health*, Vol. 17, No. 78, 2015, p. 328.

[5] Lamancusa, J. S., and Daroux, P. A., "Ray Tracing in A Moving Medium with Two-Dimensional Sound Speed Variation and Application to Sound Propagation Over Terrain Discontinuities." *J Acoust Soc Am*, Vol. 93, 1993, pp. 1716–1726.

[6] Wilson, D., Nykaza, E., White, M., Swearingen, M., Pater, L., and Luz, G., "Sound Outdoors and Noise Pollution," *Handbook of Environmental Fluid Dynamics, Volume Two: Systems, Pollution, Modeling, and Measurements*, 2012, p. 203.

[7] ECAC, "ECAC.CEAC Doc. 29. Report on Standard Method of Computing Noise Contours around Civil Airports. Volume 2: Technical Guide." Tech. rep., European Civil Aviation Conference (ECAC), 2016.

[8] Franke, S. J., and W., S. G., "A Brief Tutorial on The Fast Field Program (FFP) As Applied to Sound Propagation in The Air," *Applied Acoustics*, Vol. 27, 1989, pp. 203–215.

[9] Gilbert, K. E., and White, M. J., "Application of the parabolic equation to sound propagation in a refracting atmosphere," *The Journal of the Acoustical Society of America*, Vol. 85, No. 2, 1989, pp. 630–637.

[10] Ghinet, S., Price, A., Daigle, G. A., Stinson, M. R., Grewal, A., and Wickramasinghe, V., "Atmospheric propagation of aircraft acoustic signature from high altitude," *INTER-NOISE and NOISE-CON Congress and Conference Proceedings*, Vol. 259, Institute of Noise Control Engineering, 2019, pp. 4654–4665.

[11] Casalino, D., Barbarino, M., and Visingardi, A., "Simulation of helicopter community noise in complex urban geometry," *AIAA journal*, Vol. 49, No. 8, 2011, pp. 1614–1624.

[12] Casalino, D., van der Velden, W. C., Romani, G., and Gonzalez-Martino, I., "Aeroacoustic analysis of urban air operations using the LB/VLES method," *25th AIAA/CEAS Aeroacoustics Conference*, 2019, p. 2662.

[13] Salomons, E. M., *Computational Atmospheric Acoustics*, Springer Science & Business Media, 2001.

[14] Ostashev, V. E., and Wilson, D. K., *Acoustics in moving inhomogeneous media*, 2nd ed., CRC Press, 2015.

[15] Fuerkaiti, Y., Casalino, D., Avallone, F., and Ragni, D., "Toward inclusion of atmospheric effects in the aircraft community noise predictions," *The Journal of the Acoustical Society of America*, Vol. 150, No. 2, 2021, pp. 759–768.

[16] Porter, M. B., and Bucker, H. P., "Gaussian beam tracing for computing ocean acoustic fields," *The Journal of the Acoustical Society of America*, Vol. 82, No. 4, 1987, pp. 1349–1359.

[17] Gabillet, Y., Schroeder, H., Daigle, G. A., and L'Espérance, A., "Application of the Gaussian beam approach to sound propagation in the atmosphere: Theory and experiments," *The Journal of the Acoustical Society of America*, Vol. 93, No. 6, 1993, pp. 3105–3116.

[18] Porter, M. B., "Beam tracing for two-and three-dimensional problems in ocean acoustics," *The Journal of the Acoustical Society of America*, Vol. 146, No. 3, 2019, pp. 2016–2029.

[19] Cervenỳ, V., *Seismic ray theory*, Vol. 110, Cambridge university press Cambridge, 2001.

[20] Bian, H., Fattah, R., Zhong, S., and Zhang, X., "On the efficient modeling of generic source directivity in Gaussian beam tracing," *The Journal of the Acoustical Society of America*, Vol. 149, No. 4, 2021, pp. 2743–2751.

[21] Camargo Rodríguez, O., Collis, J. M., Simpson, H. J., Ey, E., Schneiderwind, J., and Felisberto, P., "Seismo-acoustic ray model benchmarking against experimental tank data," *The Journal of the Acoustical Society of America*, Vol. 132, No. 2, 2012, pp. 709–717.

[22] Calazan, R. d. M., "Numerical enhancements and parallel GPU implementation of the traceo3d model," 2018.

[23] Pierce, A. D., *Acoustics: an introduction to its physical principles and applications*, 3rd ed., Springer, 2019.

[24] Popov, M. M., *Ray theory and Gaussian beam method for geophysicists*, Edufba, 2002.

[25] Bian, H., Fattah, R., Zhong, S., and Zhang, X., "An efficient rectilinear Gaussian beam tracing method for sound propagation modelling in a non-turbulent medium," *The Journal of the Acoustical Society of America*, Vol. 148, No. 6, 2020, pp. 4037–4048.

[26] Červenỳ, V., and Hron, F., "The ray series method and dynamic ray tracing system for three-dimensional inhomogeneous media," *Bulletin of the Seismological Society of America*, Vol. 70, No. 1, 1980, pp. 47–77.

[27] Popov, M., Pšenčík, I., and Červenỳ, V., "Computation of ray amplitudes in inhomogeneous media with curved interfaces," *Studia Geophysica et Geodaetica*, Vol. 22, No. 3, 1978, pp. 248–258.

[28] Fuerkaiti, Y., Grande, E., Casalino, D., Avallone, F., and Ragni, D., "Efficient low-fidelity aeroacoustic permanence calculation of propellers," *Aerospace Science and Technology: Under Review*, 2022.

[29] Casalino, D., van der Velden, W. C., and Romani, G., "Community noise of urban air transportation vehicles," *AIAA Scitech 2019 Forum*, 2019, p. 1834.

[30] Casalino, D., "Reprint of: Benchmarking of Different Wave Models for Sound Propagation in Non-Uniform Flows," *Procedia IUTAM*, Vol. 1, 2010, pp. 163–172.

[31] Casalino, D., "Finite element solutions of a wave equation for sound propagation in sheared flows," *AIAA journal*, Vol. 50, No. 1, 2012, pp. 37–45.

[32] Casalino, D., Santini, S., Genito, M., and Ferrara, V., "Rocket noise sources localization through a tailored beam-forming technique," *AIAA journal*, Vol. 50, No. 10, 2012, pp. 2146–2158.

[33] Snyder, J. P., *Map projections–A working manual*, Vol. 1395, US Government Printing Office, 1987.

[34] Serafini, J., Bernardini, G., Grignaffini, G., Modini, S., and Gennaretti, M., "Acoustic wave three-dimensional ground reflection and bouncing," *Applied Acoustics*, Vol. 180, 2021, p. 108110.